pp 627–650. © Royal Aeronautical Society 2016
doi: 10.1017/aer.2016.13

Numerical simulation of wing vortex generators – methodologies and validation

M. Zastawny
mzastawny@ara.co.uk
Aircraft Research Association
Bedford
UK

ABSTRACT

This paper presents the results of a study of different Vortex Generator (VG) modelling approaches that have been performed in order to develop a better understanding of the current Computational Fluid Dynamics (CFD) capability to simulate transonic flows where wing-mounted VGs are present.

The practicality of using CFD methods commonly employed in the aerospace industry to predict the influence of VGs on wing performance is studied. It is hoped that presenting the experience gained will be of value to aerodynamicists working on similar problems in industry. An approach, using fully resolved, conformal mesh around the VGs, has been investigated through studying Reynolds-Averaged Navier Stokes (RANS) simulations with two alternate turbulence models, the Spalart-Allmaras (SA) model and the Speziale-Sarkar-Gatski (SSG) Reynolds Stress Model. An initial assessment of two alternative VG modelling techniques, use of the Chimera overset meshing and a reduced-order VG model has also been performed. In addition, an investigation of the impact of the wing deformation under aerodynamic loading was conducted. The results obtained were compared with the wind-tunnel measurements acquired in the Aircraft Research Association Transonic Wind Tunnel, using the N47-05 half model with installed VGs.

It was observed that the VGs significantly modify the flow behaviour at sufficiently high incidence, which leads to higher lift coefficient values. While the SA turbulence model was unable to capture the complicated nature of the flow when VGs were present, SSG simulations yielded promising results.

Each of the VG modelling approaches has shown some strengths and weaknesses. Further study on the subject is suggested in order to develop best practices that can be applied for solutions of industrial-scale problems.

Keywords: Vortex generators; Reynolds-stress model; wind tunnel; data comparison

Received 11 February 2015; revised 9 August 2015; accepted 3 September 2015.

NOMENCLATURE

c_f	skin friction coefficient
c_p	pressure coefficient
C_L	lift coefficient
h_{vg}	vortex generator height
M_∞	free-stream Mach number
Re	Reynolds number
SAO	Spalart-Allmaras turbulence model
SSG	Speziale-Sarkar-Gatski/Launder-Recce-Rodi turbulence model
VG	vortex generator
α	incidence angle

1.0 INTRODUCTION

This paper presents details of the investigation of Vortex Generator (VG) simulation strategies, performed at the Aircraft Research Association (ARA), as a part of the Airbus-led, UK TSB-funded ExpAero project. During the course of the programme, wind tunnel test campaigns were conducted at the European Transonic Wind tunnel (ETW) and ARA Transonic Wind Tunnel (TWT) facilities using the N47-05 half model. This model is a modification of the HiReTT model[1]. In addition, a large number of Computational Fluid Dynamics (CFD) simulations were performed at ARA for validation purposes. The analysis of combined experimental and numerical data sets offers an opportunity to gain an in-depth insight into the observed aerodynamic effects, as well as increasing confidence levels for application of CFD in virtual design studies.

Development of efficient VG simulation strategies is important, as application of VGs is a popular technique for controlling the shock-induced boundary-layer separation. Even though VGs are small devices, their impact on aircraft aerodynamic properties can be significant, especially at high angles of attack[1].

Most often, VGs are small vanes acting as lifting surfaces, with their trailing vortex flowing over the wing (Fig. 1). In principle, the vortex shed from the VG enables a redistribution of the existing momentum in the boundary layer so that higher momentum fluid is transferred closer to the wall, thus inhibiting separation. This allows the aircraft to operate efficiently over a wider range of flow conditions.

In practice, VGs usually form co-rotating or counter-rotating arrays distributed over the span of the wing. When designing a VG array, one has to consider the precise location of the VGs, their height and local angle of incidence. The complex nature of the interaction between the generated vortices and the baseline flow makes the choice of an appropriate VG array a complicated process. Use of modern CFD techniques can offer a valuable insight into the flow behaviour and allow the most suitable VG arrangement to be determined.

Despite the recent increase in computational speed and developments of numerical techniques, CFD simulations with VGs are still time-consuming and labour intensive, as VG modelling requires modifications to the baseline aircraft geometry. In addition, the small size of the devices poses additional difficulties during the mesh generation process. Furthermore, due to the complicated nature of the underlying flow, choice of an appropriate turbulence model is also of importance. An excellent review of subsonic VG modelling methods is presented in Ref. 3, while some work on VGs in transonic flows include Refs 4 and 5.

https://doi.org/10.1017/aer.2016.13 Published online by Cambridge University Press

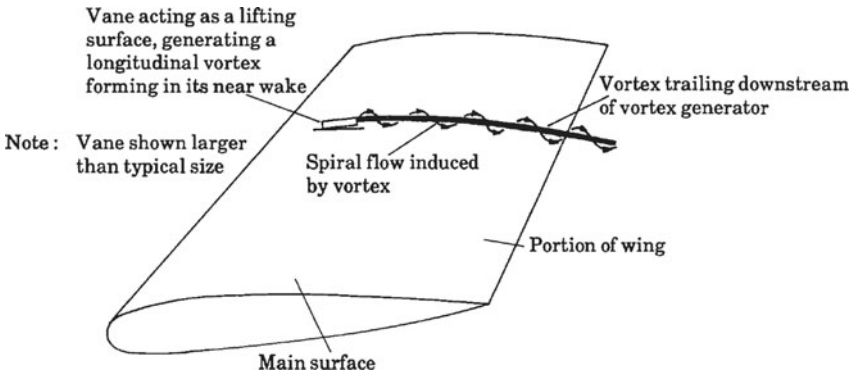

Figure 1. A sketch of a VG-induced vortex trailing over the wing surface[2].

The study presented in this work is focused on the assessment of alternate VG modelling methodologies. This is achieved by simulating flows over a wing equipped with an array of six vane VGs. The principal methodology investigated is a fully resolved, conformal mesh approach with an assessment of the impact of the chosen turbulence model.

In addition, two alternative modelling strategies are studied. The first technique involves application of the Chimera method to generate an overset mesh block in the region around each VG, while the second uses a reduced-order VG model to indirectly simulate the impact that the VGs have on the flow behaviour.

The simulation results are compared with data acquired during the wind-tunnel test campaign in the ARA TWT. The analysis of the clean wing simulations presented in Ref. 6 shows that, despite being small, model deformation in the TWT is not insignificant in the current context. Hence, computations in which wing bend and twist under load are taken into account have also been performed.

The paper is structured as follows: Section 2 provides an overview of the wind tunnel tests and describes the chosen VG configuration. This is followed by the description of the CFD set-up in Section 3. The approach when the VGs are modelled using a conformal mesh is presented in Section 4, while discussion of alternative VG modelling strategies is given in Section 5. The paper finishes with conclusions from the performed study.

2.0 WIND-TUNNEL TEST

Experimental test campaigns were conducted at ETW and ARA TWT wind-tunnel facilities, as a part of the ExpAero project. During both of the test campaigns, a number of VG configurations were tested. This section presents an overview of the wind-tunnel test set-up and the obtained results, which form a reference to the subsequent CFD analysis.

Although the cryogenic ETW wind tunnel offers a unique ability to conduct experiments at high Reynolds numbers, it is expensive and requires significant overhead time when different model configurations are analysed, which is a typical situation for a study of VG arrays. ARA TWT, on the other hand, offers an easy access to the model in the wind tunnel throughout the test campaign, therefore allowing for a much larger number of configurations to be tested within a similar time scale.

https://doi.org/10.1017/aer.2016.13 Published online by Cambridge University Press

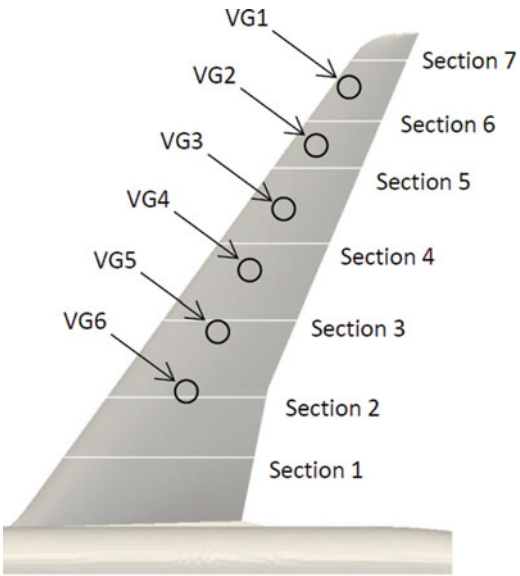

Figure 2. (Colour online) VG positions relative to the pressure tap sections.

A total number of 13 different VG configurations were studied in the course of the ARA test campaign and the one judged to be of particular interest was chosen for the subsequent CFD analysis. Each configuration was defined by a number of VGs with specified heights positioned on pre-defined locations on the wing.

The tests in the TWT were conducted at a nominal Mach number of $M_\infty = 0.85$, with a move and pause traversing over a range of incidences from $-10°$ to $+10°$, for all the investigated VG array arrangements. During each test, pressure measurements at seven span-wise stations were taken. Additionally, oil-flow visualisations were generated for the clean wing and configurations of special interest at incidence $\alpha = 3.5°$.

Out of the investigated VG array arrangements, the most promising one contained six vanes with 1.3 mm height. The positioning of the VGs relative to the pressure tap stations is illustrated in Fig. 2. Note that Section 1 (the most inboard section) has no neighbouring VG; therefore, it is expected that the pressure distribution for this section should remain approximately the same for the clean wing configuration and when the VG vanes are attached. On the other hand, Sections 5 and 6, for example, are positioned on both sides of VG2; therefore, they are expected to be strongly affected by the VG presence.

As an atmospheric wind tunnel, the TWT has a limited Reynolds number range, defined by the flow speed and the model dimensions. In the current tests, the nominal Reynolds number, based on the aerodynamic mean chord, was $Re_{\text{nom}} = 5.3 \times 10^6$; therefore, an appropriate transition setting was necessary in order to obtain boundary-layer behaviour similar to that experienced in the high Reynolds number tests in ETW. This was achieved by applying a span-wise line of trip dots on both upper and lower surfaces of the wing. The chord-wise position of the transition line is summarised in Table 1.

The details of the results obtained and their comparison with the CFD data are presented in Section IV.

https://doi.org/10.1017/aer.2016.13 Published online by Cambridge University Press

Table 1
Transition fixing for $Re = 5.3M$

Component	Wing root	Crank	Wing tip
Transition	12% chord	15% chord	15% chord

Table 2
Mesh characteristics

Configuration	No of points	FCH
CLEAN	3.6M	5.0e-7
VG	3.8M	5.0e-7

Table 3
Solver set-up summary

Incidences	0.0°, 2.0°, 3.0°, 3.5°
Mach number	0.85
Reynolds number	$5.3M$
Solver discretisation	2nd order central scheme
Relaxation Solver	Backward Euler
Multigrid	3w

3.0 CFD SET-UP

The work presented in this report exclusively employed numerical meshes generated with SOLAR[7] and all numerical flow solutions were obtained using the TAU Reynolds-Averaged Navier Stokes (RANS) solver[8].

3.1 Aircraft model

The baseline mesh and geometry used during the current study was generated using the Computer Aided Design (CAD) data of the N47-05 aircraft model utilised during the wind-tunnel experiments. Since the current study employs the ARA TWT wind-tunnel test results as the reference, a mesh was generated for the wind-tunnel scale, i.e. $Re = 5.3 \times 10^6$ (see Table 2 for mesh characteristics).

3.2 Solver settings

The RANS solver settings applied during the simulations are summarised in Table 3. Two different turbulence models, the original Spalart-Allmaras one-equation model (SAO)[9] and the SSG/LRR Reynolds-stress model (SSG)[10], were utilised during the simulations.

Computations were performed for a constant Mach number of $M_\infty = 0.85$ and the nominal Reynolds number used in the wind tunnel during the TWT test campaign. Transition was set during the simulations in order to mimic the transition setting adopted in the TWT, see Table 1.

https://doi.org/10.1017/aer.2016.13 Published online by Cambridge University Press

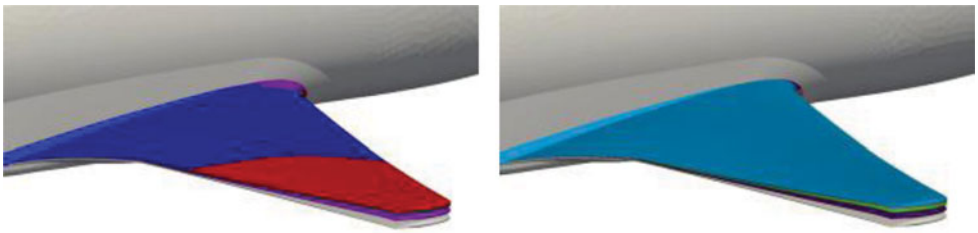

(a) Clean wing (b) Wing with VGs

Figure 3. (Colour online) Estimated model deformations at TWT flow conditions.

3.3 Deformation estimation

In the analysis of the clean wing simulation results presented in Ref. 6, it has been shown that the wing deformation is an important factor affecting the flow characteristics. Since the deformation increases with the wing loading, larger deformations are expected at high angles of attack, which is the main region of interest of the study presented in this paper.

The wing bending and twisting experienced by the model during the test campaign in TWT is unknown; however, the deformation measurements are available for the ETW experiments. Since the same model has been used in both test campaigns, it was anticipated that its structural behaviour is similar under load and only marginal differences, due to temperature variations, are present.

Therefore, the wing stiffness can be derived, based on the known aerodynamic loading and the deformation measured at $Re = 32.5 \times 10^6$ during the ETW test campaign. It is then possible to combine the wing structural properties and the loading measured at TWT to estimate wing deformation in the ARA wind tunnel.

The approach discussed above is applied for different angles of attack. The overall deformation of the wing is shown in Fig. 3, while the span-wise twisting distribution is illustrated in Fig. 4. It can be observed that the twist is essentially the same for both the clean wing and the wing with attached VGs for incidences up to $\alpha = 2.0^\circ$. The situation is more complicated for higher angles of attack. Whereas, in the case with VGs, the deformation continues to increase withα– the clean wing is actually less deformed at $\alpha = 3.0^\circ$than at $\alpha = 3.5^\circ$. This is due to the boundary-layer separation effects, which reduce the wing loading at higher incidences. The overall difference between twist of the wing tip for the clean wing configuration and the wing with VG configuration at $\alpha = 3.5^\circ$ is approximately $\Delta\alpha = 0.15^\circ$.

4.0 RESOLVED VG ANALYSIS

The main approach, adopted during the presented study, uses a resolved, conformal mesh around the VGs. Although this technique allows for a direct simulation of the flow around the VGs, it has a number of disadvantages such as:

- Necessity to modify the baseline mesh in order to include the VG geometry,
- Difficulties associated with setting appropriate mesh refinement around the VGs,
- Time-consuming modifications to the vane geometry and positioning.

https://doi.org/10.1017/aer.2016.13 Published online by Cambridge University Press

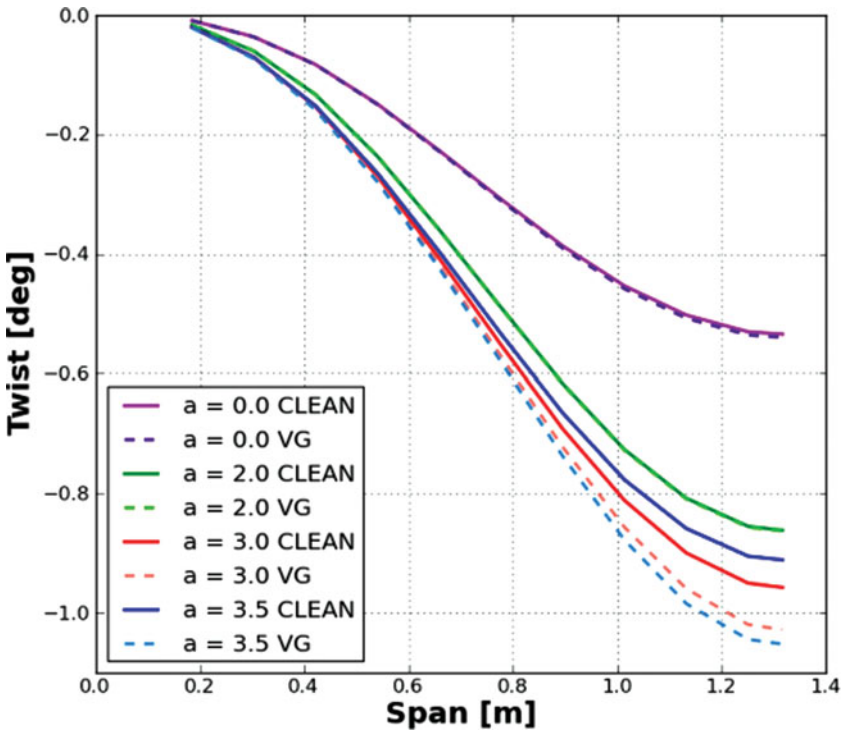

Figure 4. (Colour online) Estimated model twist at different incidences for TWT flow conditions.

Nonetheless, using a resolved mesh around the VGs is likely to be the most accurate approach, provided a mesh of sufficient quality can be generated.

4.1 Methodology

The VG configuration geometry was generated by modification of the existing baseline clean wing. Additional surfaces were inserted in locations corresponding to the VG positions in the wind-tunnel experiments in order to create trapezoidal vanes.

The mesh generation process involves specifying additional refinement in the vicinity of the inserted VGs, which is controlled mainly by the number of desired cells across the VG thickness. Setting the refinement parameters requires trial and error in order to obtain a mesh of sufficiently high quality. It is also worth noting that a structured mesh was generated on all of the VG faces, as allowed by the functionality of SOLAR.

The slices through the volume mesh at various VG heights (h_{vg}) behind the VG trailing edge are shown in Fig. 5. It can be observed that a structured mesh, with two grid cells across the VG thickness, was generated on the VG surface. The near-field mesh experiences a strong pull-back in the region near the vane; however, its thickness is nearly recovered at five VG heights behind the vane trailing edge. This is especially important for SSG simulations, as it has been shown that this turbulence model is very sensitive to the thickness of the near-field layer mesh[11].

https://doi.org/10.1017/aer.2016.13 Published online by Cambridge University Press

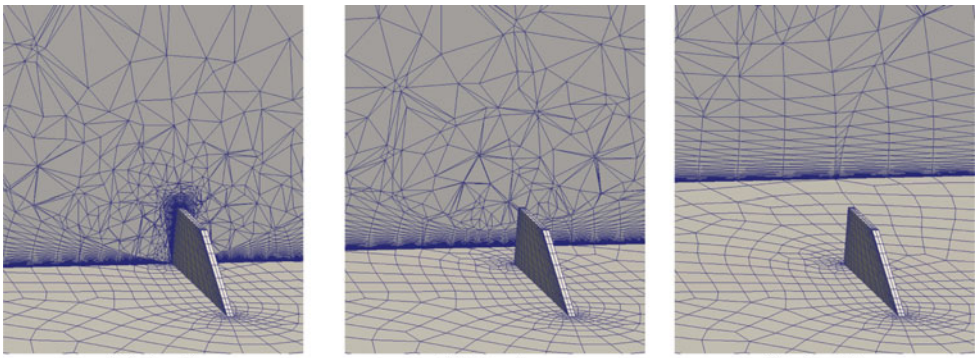

Figure 5. (Colour online) Volume mesh slices at different distances (***d***) behind the VG trailing edge.

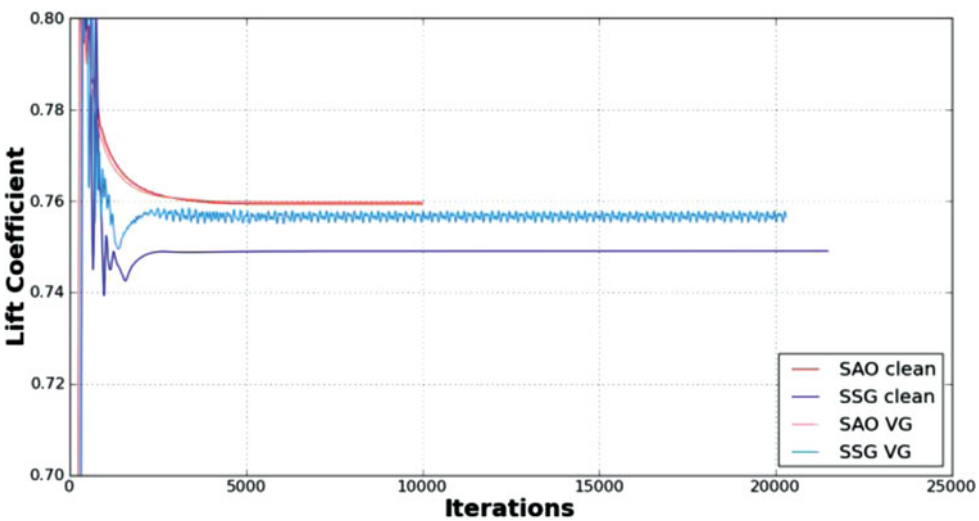

Figure 6. (Colour online) Typical convergence history for the simulations at $\alpha = 3.5°$.

4.2 Un-deformed wing results

During the initial stage of the study, lift polars were computed for both the clean wing configuration and for the wing with attached VGs, using both SAO and SSG turbulence models. As initial results from the SAO model gave a poor performance, which was likely due to the inappropriateness of the eddy viscosity hypothesis for vortex modelling, it was decided to not examine a two-equation eddy viscosity model, such as k-ω SST.

The clean wing simulations converged to the specified convergence limits regardless of the chosen turbulence model. On the other hand, C_L oscillations are observed in the convergence history for simulations with VGs at high angles of attack $\alpha = 3.5°$ (see Fig. 6 for a representative convergence history plot). The lift coefficient predicted by the SAO model is $C_L = 0.784 \pm 0.004$, and for the SSG model is $C_L = 0.780 \pm 0.005$. This corresponds to an uncertainty of around $\pm 0.5\%$ for both turbulence models. Because of the small uncertainty levels, some information about general flow behaviour can still be extracted from the obtained

https://doi.org/10.1017/aer.2016.13 Published online by Cambridge University Press

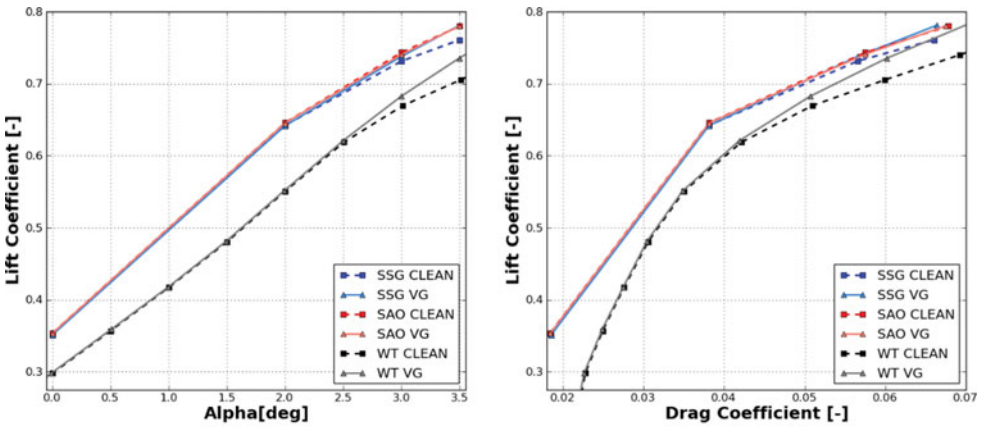

Figure 7. (Colour online) Force coefficient polars for the simulated model.

solutions. Still, a level of variability is expected in the obtained results and has to be taken into account (see Ref. 12 for details). Note that the analyses presented in this paper are based on the results from the final iteration of each TAU simulation.

The lift-and-drag polars obtained during the CFD simulations, along with the referenced wind-tunnel data, are illustrated in Fig. 7. Regardless of the chosen turbulence model and whether VGs are present, the predicted lift coefficient remains virtually identical up to the onset of separation estimated at $\alpha = 2.0^\circ$, which agrees with observations presented in the clean wing study[6].

Differences in the calculated C_L value can be observed for higher incidences. While the SAO model predicts the same value of lift coefficient with and without VGs, a clear impact of the VG array presence is observed when the SSG model is employed. It is worth noting, however, that a significant difference between the turbulence models is observed in the clean wing simulations, as the C_L obtained with the SSG model is considerably lower than that from the SAO model. This indicates that the SAO model does not successfully capture the flow behaviour at large angles of attack. These observations are in line with the results of the HGR-01 aerofoil at stall simulations presented in Ref. 10, in which neither of the turbulence models was able to match the experimental results, but the SSG solution was noticeably closer.

The drag polar shown in Fig. 7(b), indicates that the VGs are reducing the drag coefficient at a higher lift coefficient. This holds both for the SSG simulations and the wind-tunnel measurements. More details about the flow behaviour can be extracted upon inspection of the skin friction coefficient plots and oil flow photographs at $\alpha = 3.5^\circ$, shown in Fig. 8. The c_f distributions obtained with the SAO model strongly differ from the SSG results for both configurations. The figure clearly indicates a completely separated outboard wing flow behind the shock for the clean configuration simulated with the SAO model, and a much more complicated but less separated flow structure observed for the SSG simulations. Furthermore, it is quite obvious that the SAO model fails to capture the global effects of the VGs, as the flow behaviour is modified only in the outboard region of the wing. The SSG model, in contrast, produces flow patterns much closer to the ones observed in the oil flow pictures taken during the wind-tunnel test campaign. The vortices shed from the VGs result in a more energetic boundary layer, which is less prone to separation.

https://doi.org/10.1017/aer.2016.13 Published online by Cambridge University Press

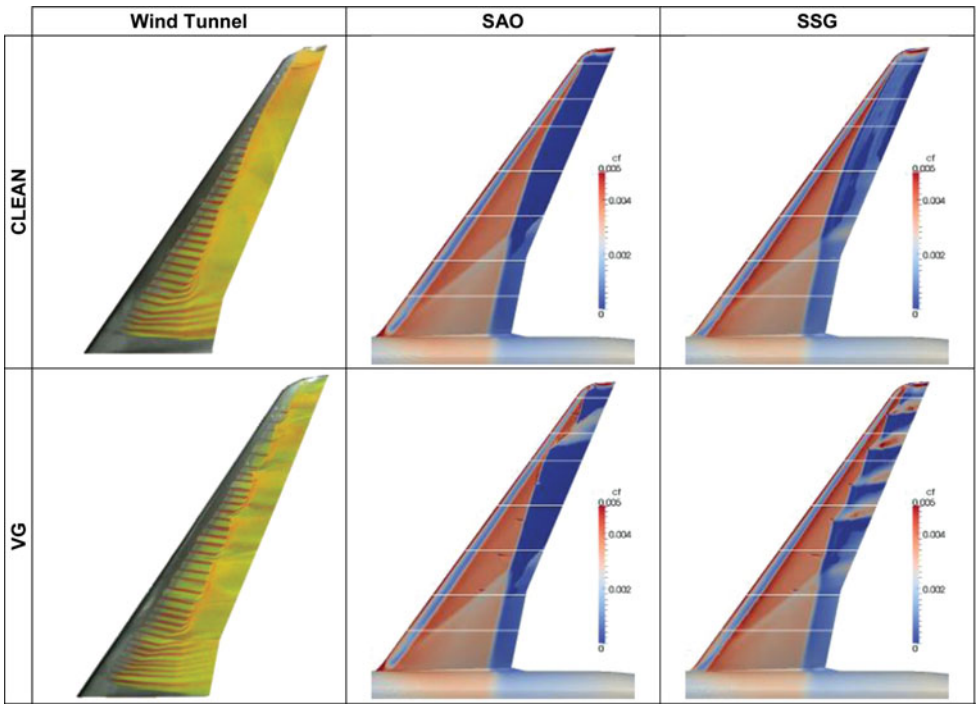

Figure 8. (Colour online) Wind-tunnel oil flow photographs and CFD skin friction distributions at $\alpha = 3.5°$.

The pressure distribution profiles shown in Fig. 9, allow for a more quantitative analysis to be conducted. The clean wing pressures are significantly different for the two turbulence models. The shock location predicted by the SSG model is upstream of the one observed in the SAO simulation for the clean configuration. This is one possible explanation for the reduced lift computed with the SSG model, even though the SSG results predict smaller boundary-layer separation. Moreover, a very strong region of separation is observed near the trailing edge with the SAO model, resulting in additional lift generated by the wing.

Inspection of the pressures with VGs shows a number of interesting features. In general, the aft shock movement predicted by the SSG model agrees with the wind-tunnel observations, while no clear pattern in the SAO solutions can be identified. Also, the impact of the VGs on the lower surface pressures is captured in the SSG results, but not in the SAO simulation. Both models, however, predict different trailing-edge pressure to that measured during the wind-tunnel test campaign. This is probably due to the fact that deformation is not considered in this case, and it is expected that the results will be closer to the experiment when the deformation is taken into account.

In addition to the aforementioned simulations, a test to assess whether the mesh refinement had a significant effect on the obtained flow solutions was performed by adding the VG sources to the clean wing geometry, i.e. local refinement of volume mesh without addition of VG surfaces. The results indicate that, while there was some impact on the SAO solutions, the SSG simulations were indifferent to the addition of VG sources. A polar was also simulated and is shown in Fig. 10, where the VG mesh contained four cells across the vane thickness rather than two cells as in the standard mesh,. The fact that small differences are observed

https://doi.org/10.1017/aer.2016.13 Published online by Cambridge University Press

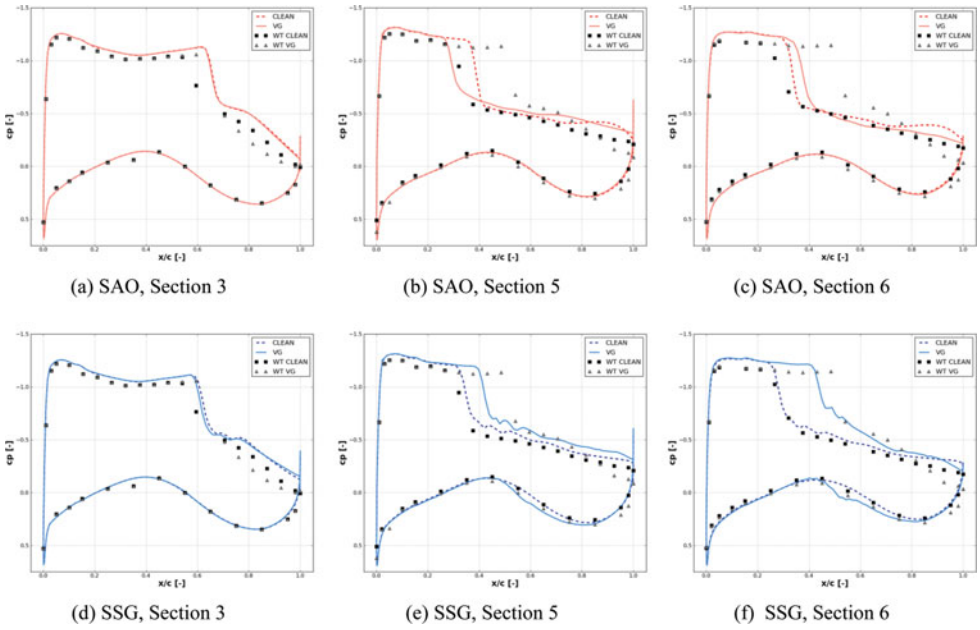

Figure 9. (Colour online) Pressure distributions obtained with different turbulence models at $\alpha = 3.5°$.

between the results obtained with different meshes, when compared to the overall difference between the clean wing and VG configurations, justifies the observations made in this paper.

4.3 Deformed wing results

The solutions presented in the previous section used the un-deformed wing as the baseline geometry. However, at high incidences, the aero-elastic effects significantly contribute to the flow behaviour, changing its character, especially on the outboard portions of the wing. Therefore, simulations in which the wing deformation is included are necessary in order to obtain a more quantitative comparison with the wind-tunnel measurements.

The modified wing shape was estimated, based on the approach outlined in Section 3. The calculated bend-and-twist were used as inputs to a TAU process that generated a new, deformed computational grid.

As in the case of the previously presented analyses, two turbulence models (SAO and SSG) were employed to simulate flows past a clean wing and the wing with attached VGs. A polar was generated for each run. Since the wing shape was different at every angle of incidence, each simulation was initialised with free-stream conditions, which led to longer convergence times.

As before, the SSG simulation with VGs did not converge fully and high-frequency oscillations in the lift coefficient at high incidences were encountered. The magnitude of the fluctuations is similar to the un-deformed case and is equal to $\pm$ 0.2% of the average lift coefficient value. Still, the SSG model is able to capture some of the VG impact on the flow, which is indicated by the different C_L value.

Lift and polars generated for the deformed wing are shown in Fig. 11. It can be observed that, even though the predicted lift-and-drag coefficient values are closer to the experimental

https://doi.org/10.1017/aer.2016.13 Published online by Cambridge University Press

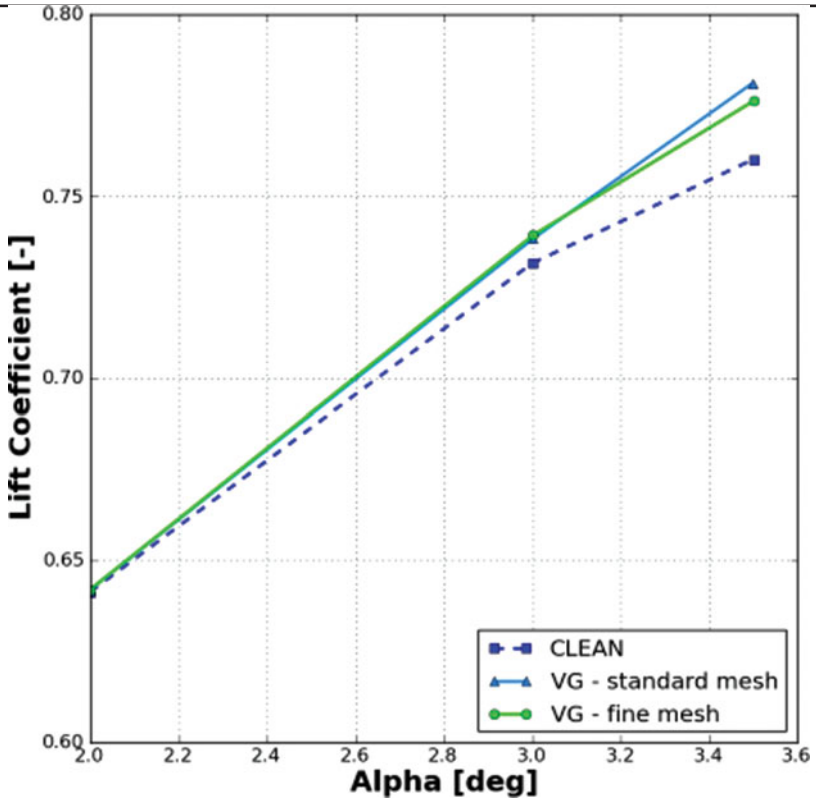

Figure 10. (Colour online) Lift coefficient polar for the SSG simulations with different VG grid refinement levels.

measurements, there are differences throughout the incidence range between the wind tunnel data and simulated coefficients. Explanations for this fact are explored in Ref. 6, and the most plausible causes can be summarised as:

- Wind-tunnel wall interference and its influence on the flow past the half-model,
- Local junction separations at the wing root during the wind-tunnel test,
- Limited accuracy of the deformation prediction method,
- Limited ability of the CFD to capture accurately flow behaviour at large angles of attack.

Nevertheless, current results show that the wing deformation under aerodynamic loads is an important factor and cannot be omitted in this type of study.

Focusing on the simulations obtained, it can be concluded that both turbulence models perform nearly identically up to $\alpha = 2.0°$, where the onset of separation is identified. No VG influence on the forces is visible for low incidences. Their impact, however, starts to emerge for higher angles, although it is only captured by the SSG model, which is in line with the observations made in the previous section.

The SSG turbulence model results indicate that the predicted lift coefficient increase, caused by application of VGs, is smaller than for the un-deformed case. This is indeed confirmed by Fig. 12, where the change of the lift coefficient induced by the VGs is shown. Although, when the deformation is considered, ΔC_L is expected to be closer to the

https://doi.org/10.1017/aer.2016.13 Published online by Cambridge University Press

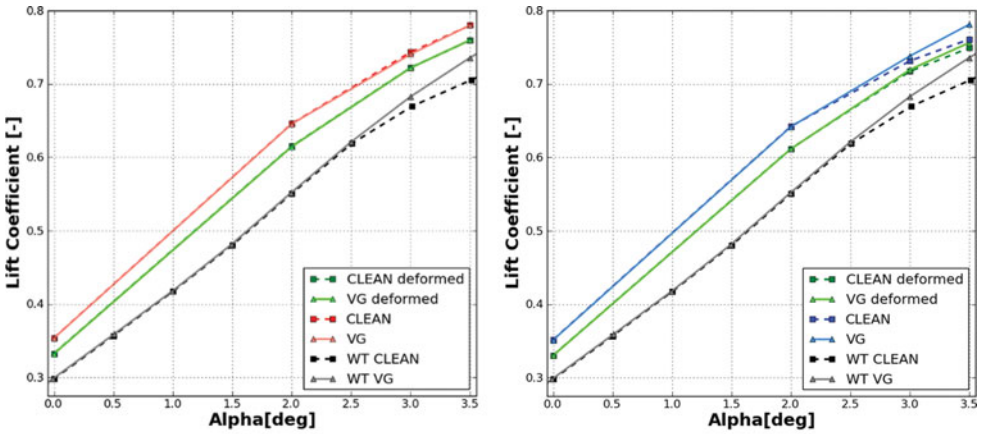

Figure 11. (Colour online) Lift coefficient polars for the simulations with a deformed model.

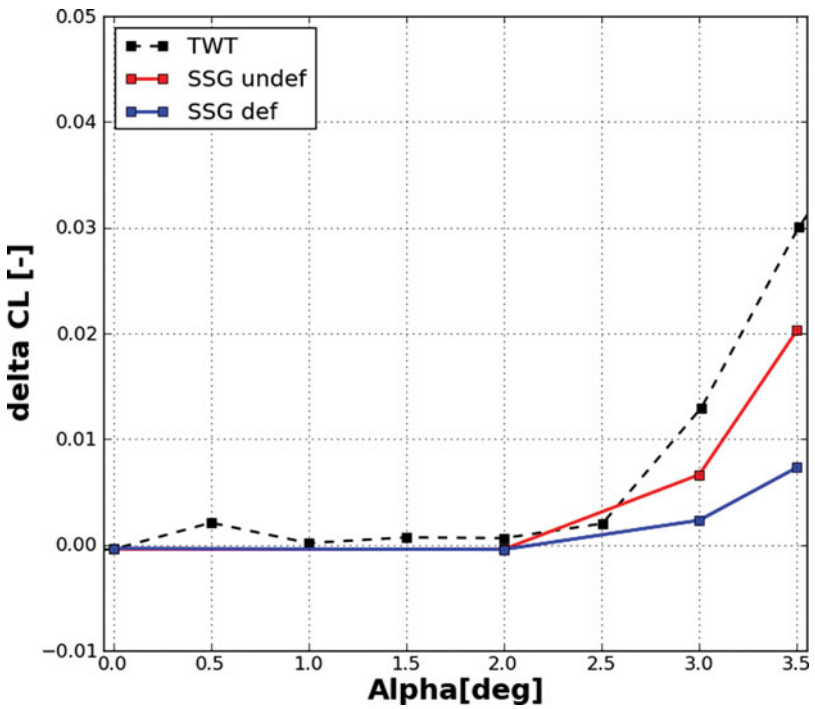

Figure 12. (Colour online) Change in the lift coefficient due to application of the VGs.

experimental measurements, the opposite is true. The polar data seems to indicate, however, that the difference is more likely to be a result of inaccuracies in the clean wing behaviour prediction.

The skin friction distribution plots shown in Fig. 13 differ strongly from their equivalents (Fig. 8), obtained when the deformation was not considered. While the SAO model predicts

https://doi.org/10.1017/aer.2016.13 Published online by Cambridge University Press

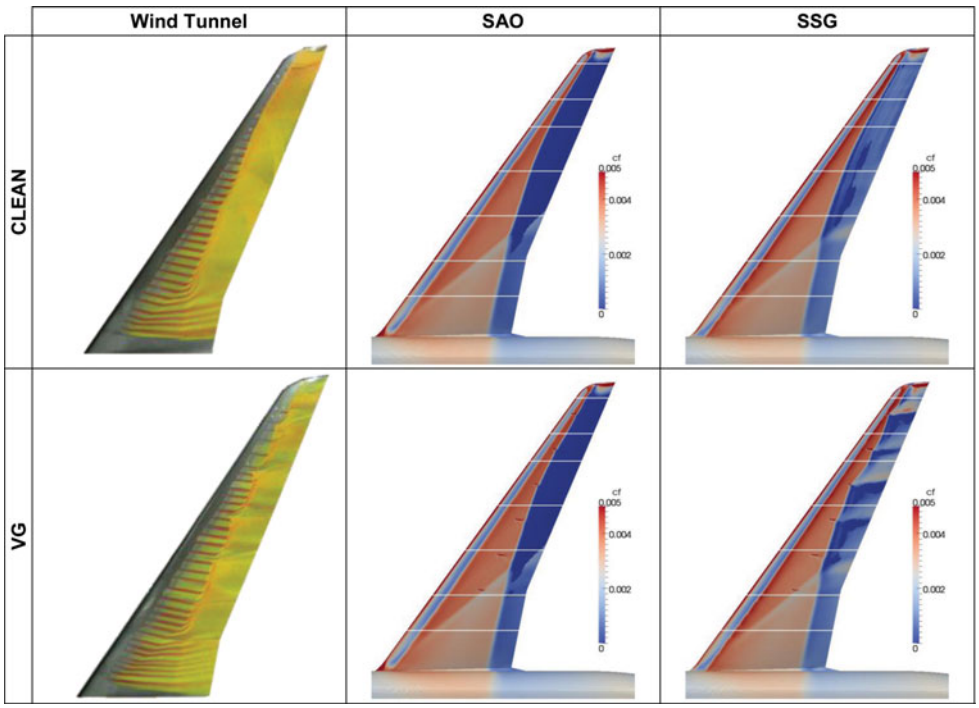

Figure 13. (Colour online) Wind-tunnel oil flow pictures and CFD skin friction distributions obtained during deformed wing simulations at $\alpha = 3.5°$.

a fully separated outboard flow behind the shock for both configurations, the SSG turbulence model leads to much more complicated flow behaviour. The clean wing flow is widely attached with only small regions of separation visible in the skin friction image. On the other hand, the impact of the application of VGs can be easily identified by the presence of clear vortex trails. The boundary layer behind the VG vanes is, however, less energetic than the un-deformed simulations presented earlier, which is indicated by lower values of the skin friction coefficient c_f.

The quantitative analysis offered by the inspection of pressure distributions shown in Fig. 14 allows for a better understanding of the flow behaviour. Firstly, it can be observed that the CFD predictions do not match the data acquired during the wind-tunnel test. Although the suction peak c_p values are generally in a good agreement with the experiments, the shock position remains different both in the SAO and SSG results. For the clean wing simulations, the shock is located aft of the experimental measurements; however, its downstream movement, when the VGs are present, is not captured to the full extent. Focusing on the SSG results, it can be observed that the trailing-edge pressures computed with this turbulence model are similar to the experimental values for all configurations at Section 5, but only for the clean wing at Section 6. In other cases, the CFD predicts trailing-edge separation when none is observed in the wind tunnel. Section 5, however, shows an encouraging result, as the pressure distribution from the VG simulation is in line with the experimental measurement.

The analysis of the pressure distributions seems to indicate that the main limitation of the current study is the fact that the clean wing simulations are not similar to the experimental

https://doi.org/10.1017/aer.2016.13 Published online by Cambridge University Press

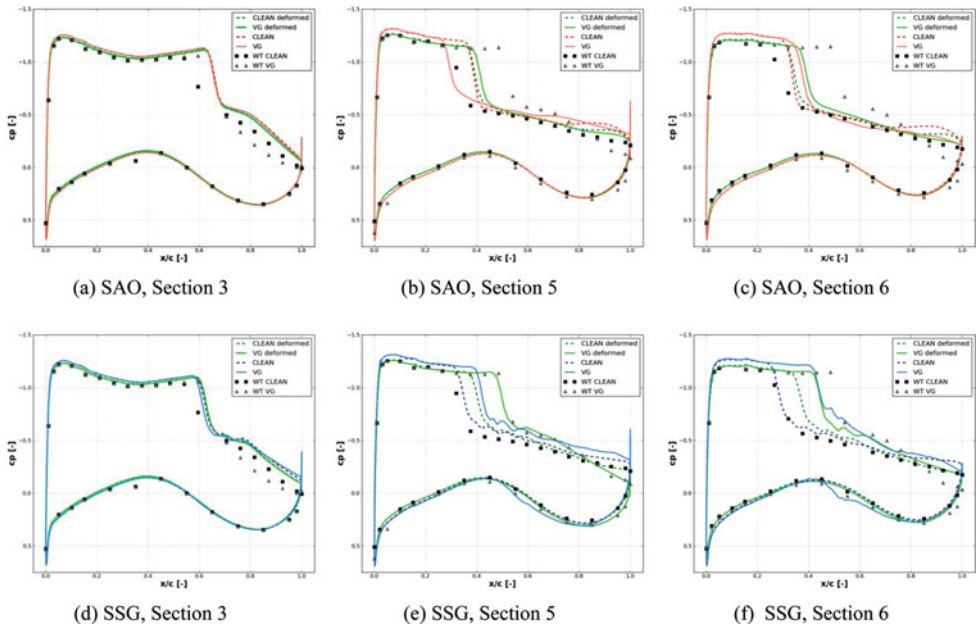

Figure 14. (Colour online) Pressure distributions obtained with different turbulence models during deformed wing simulations at $\alpha = 3.5°$.

data. As was stated before, CFD solutions are expected to encounter problems when large incidences are considered, even if the SSG turbulence model is adopted. Nevertheless, the behaviour of the VG simulations seems to indicate that it is possible to simulate the VGs with the SSG turbulence model and to obtain reasonable flow prediction.

5.0 ALTERNATIVE MODELLING STRATEGIES

Modelling the VGs with a fully resolved, conformal mesh is a time-consuming process. Moreover, each time the VG geometry or the array arrangement is modified the entire computational set-up has to be changed as well. It is, therefore, beneficial to adopt a different, more efficient approach that would allow the VGs to be simulated without a significant penalty on the accuracy of the solution. Two different alternatives to the fully resolved, conformal mesh approach are studied here. These techniques are:

- Application of Chimera method to generate an overset mesh block in the region around each VG
- Reduced-order VG model

Details of the methods and results obtained are discussed below. Since the results presented in the previous section indicate that only the SSG model is capable of capturing the impact that VGs have on the flow behaviour, only this turbulence model is used in the subsequent analysis.

https://doi.org/10.1017/aer.2016.13 Published online by Cambridge University Press

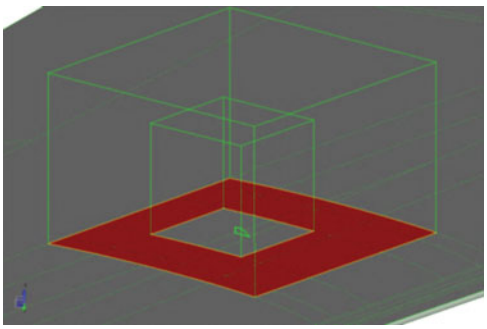

Figure 15. (Colour online) The chimera block and the hole in the baseline grid.

5.1 Chimera method

An alternative to conformal meshing for the fully resolved mesh around the VGs is to adopt the Chimera method, which employs an unmodified base mesh superposed with an overset Chimera block, used to generate a refined mesh around the VG vanes. In this approach, the VGs are still meshed directly; however, their mesh can be largely decoupled from the baseline wing mesh.

Due to its unique ability to combine independent meshes, Chimera meshing appears to be a promising approach for modelling flows with VGs. Some advantages of this technique are:

- Once the Chimera block is generated, no modifications are required to the base clean wing geometry.
- The approach allows for efficient modifications of the VG geometry inside the Chimera block.
- In theory, the mesh generation for the VG and the wing is easier and much faster than in the case of fully resolved VGs.

The work presented here shows the effects of a preliminary analysis and a feasibility study to assess whether this method can be applied to the simulations of wings with VGs. Since only an initial study has been performed, it was decided to apply the Chimera technique to model only one of the simulated VGs. The second outboard vane was chosen (VG2), as it is expected to provide the most valuable insight into the properties and performance of the technique. All remaining VGs were meshed using the same mesh as in Section 4.

The process of Chimera mesh generation involves a number of steps. Initially, the model geometry is divided into the wing and the Chimera block geometries. Then, additional faces are generated, corresponding to a hole in the base mesh and the Chimera block boundaries. Afterwards, grids for the wing and the Chimera block are generated separately and combined. Finally, the merged grid is assessed to ensure that the overlap region size and the grid refinement are adequate and allow for successful interpolation of the flow variables between the meshes. The process has iterative character, as tuning the Chimera block size and grid refinement is necessary.

As mentioned above, the first step of the process is generation of an appropriate geometry. Figure 15 illustrates the Chimera block and the hole cut in the original geometry. The choice of dimensions was driven by the fact that the hole in the baseline geometry should isolate the

https://doi.org/10.1017/aer.2016.13 Published online by Cambridge University Press

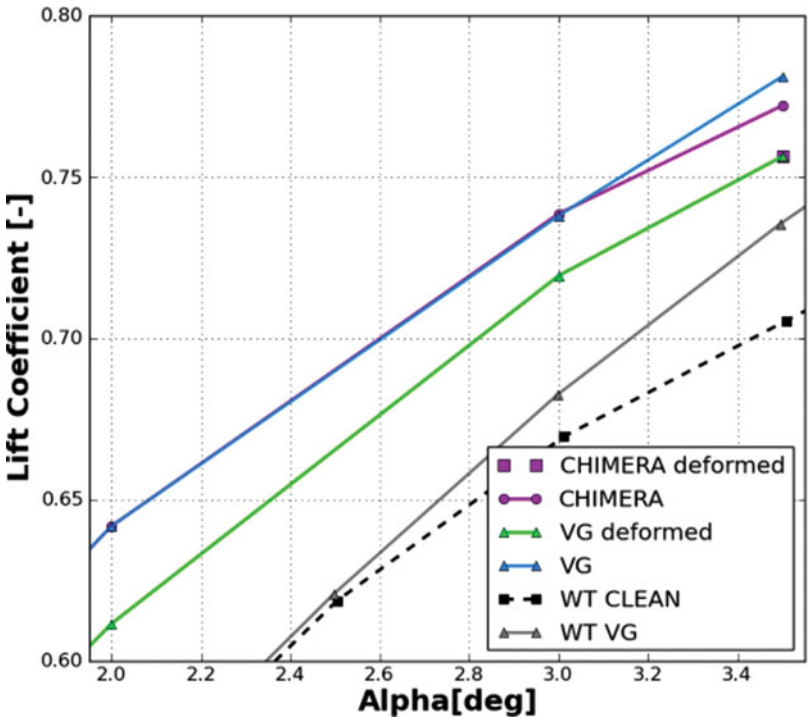

Figure 16. (Colour online) Lift coefficient polar for the simulations involving the chimera meshing.

VG from the base mesh and the Chimera block should be large enough to ensure that there are at least three cells in the overlap region. The height of the hole was set to eliminate the mesh pull-back in the baseline grid.

A polar, using the Chimera mesh, was generated for the un-deformed model; while, a single point at $\alpha = 3.5^\circ$ was computed for the deformed wing. The lift coefficient polar is presented in Fig. 16. As before, high-frequency oscillations were observed at high incidences; however, they remain small relatively to the mean lift coefficient. The computed C_L at the highest incidence for the un-deformed case differs from the conformal mesh results obtained earlier. On the other hand, the results are identical when wing deformation is considered.

Inspection of the skin friction distribution plots, presented in Fig. 17, indicates possible reasons for the observed differences. A clear impact of the application of the Chimera method can be identified for the un-deformed case. The vortex trail behind the second VG has disappeared and a region of separation has been observed instead. This leads to the loss of lift which can be seen in the polar plot. The results for the deformed case are identical to those observed in Fig. 13. This is potentially encouraging, as it indicates that the Chimera method can be successfully applied to model the VGs and offers the same quality of results as the simulations with fully resolved mesh around the VGs. However, it should be borne in mind that the impact of the deformation is to reduce the wing loading; hence, the Chimera method might still encounter problems at higher incidences.

Inspection of pressure distributions shown in Fig. 18 allows for more quantitative analysis to be performed. As expected the pressure distributions at Section 3 are nearly identical for all the cases. On the other hand, thec_p values, obtained using the Chimera meshing in the

https://doi.org/10.1017/aer.2016.13 Published online by Cambridge University Press

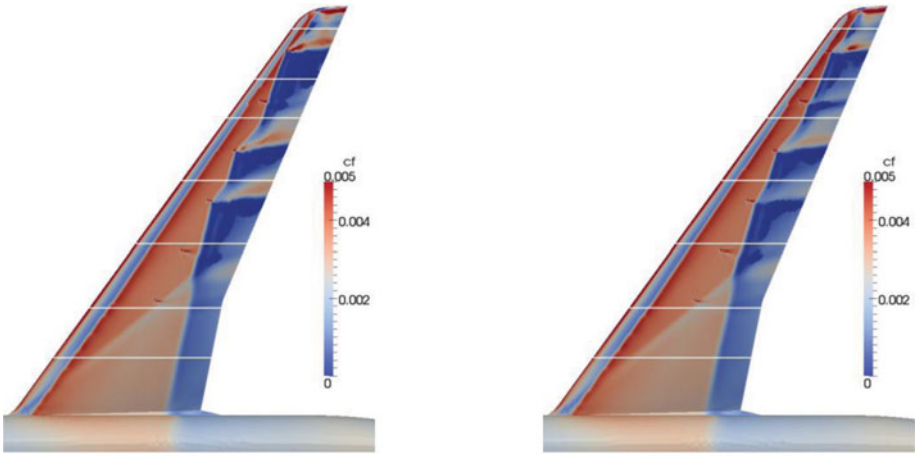

(a) undeformed wing (b) deformed wing

Figure 17. (Colour online) Skin friction distributions at $\alpha = 3.5°$ obtained using the Chimera mesh.

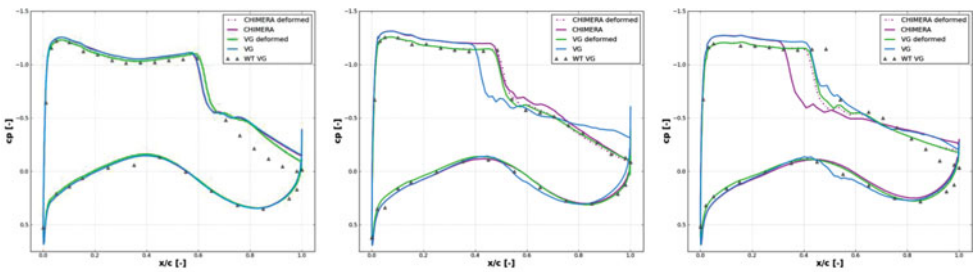

(a) Section 3 (b) Section 5 (c) Section 6

Figure 18. (Colour online) Pressure coefficent distributions at $\alpha = 3.5°$ obtained using the Chimera mesh.

un-deformed simulation, differ significantly from their equivalents at the outboard sections. A significant movement of the shock for both of the outboard sections can be observed. Interestingly, the shock motion differs from section to section, and is downstream of the resolved case in Section 5 and upstream for Section 6, with the Chimera method offering a better prediction for Section 5 and the resolved mesh for Section 6. For the deformed case, it can be clearly seen that the pressures at all sections are in line with the earlier results.

In summary, the results presented here illustrate that the Chimera method can be successfully applied as a promising alternative to a fully resolved VG technique. A deeper study is, however, necessary in order to assess the Chimera method performance when the wing loading is high.

5.2 TAU reduced-order VG model

Adaptation of both the VG modelling approaches presented above requires considerable effort in preparation of appropriate geometry and during the mesh generation process. This fact has been widely accepted and has driven effort to develop a reduced-order VG model, which would allow the influence of the VGs on the flow to be captured, without the full representation of the geometric details of the VG.

https://doi.org/10.1017/aer.2016.13 Published online by Cambridge University Press

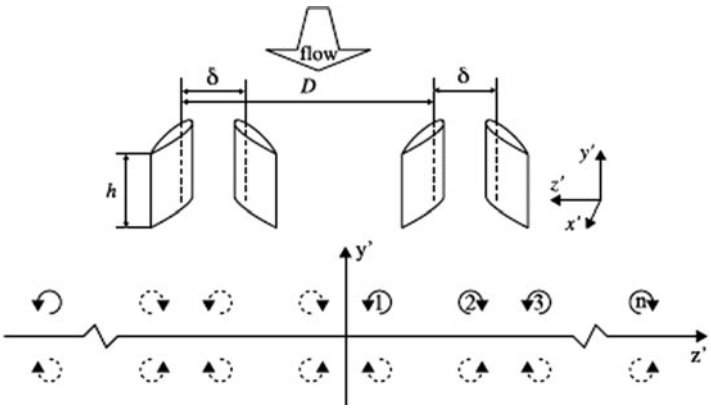

Figure 19. Geometry and flow induced by the VG array[14].

A number of reduced-order models have been presented in the literature. An overview of some of the possible techniques, with focus on large-scale applications, is presented in Ref. 3. In general, the available approaches can be divided into two groups: modelling the VG and modelling the vortex alone. In the first approach, additional forcing terms are inserted into flow equations in order to align the flow with the VG, as for example in Ref. 13. As modelling the VG directly assumes a continuous fluid domain, the resulting pressure field will not be correct. Also, some grid refinement is required in order to enhance the method accuracy.

In the latter approach, the vortex is modelled independently of the underlying VG geometry, by superposition of the base flow with the velocity profile corresponding to the modelled vortex. This is useful when the details of the flow local to the VG are less important than the downstream impact of the vortex; the local near-vortex flow-field might not be represented accurately, because only tangential velocity components are inserted. A variant of this method was developed by Törnblom and Johansson[14], who modify not only the momentum equations but also the Reynolds stress transport equations. This approach forms the basis of the reduced-order VG model currently available in TAU.

The method does not model the VGs directly. Instead, it approximates the vortices produced and adds their effect to the flow equations. The vortices are approximated by a Lamb-Oseen model, while their strengths are computed from lifting line theory. Since the VG model modifies the Reynolds stress transport equations, a simulation with the Reynolds Stress Model (RSM) is required in order to employ this technique.

Modelling of the vortices is achieved by generating a set of VG planes, defined by a number of wall points specified on wall surfaces, to which the modelled VGs are attached. Each wall point defines an infinite array of counter-rotating VG pairs (Fig. 19). The definition of the VG array contains information about the distance between the VGs in a pair (δ), vane height (h) and the distance between consecutive VG pairs (D). The incidence angle of the right hand side and left hand side vanes, their chords and some numerical parameters are also specified.

The model's parameter specification is not straight-forward, as the model definition is somewhat ambiguous and not immediately applicable to the investigated set-up. Nevertheless, a number of test cases were prepared to evaluate its performance.

Although, in principle, the model should not require any additional mesh refinement, three meshes were investigated in order to assess its grid sensitivity. The clean wing mesh without any additional sources was used as a baseline case. Two additional grids, with refinement in

https://doi.org/10.1017/aer.2016.13 Published online by Cambridge University Press

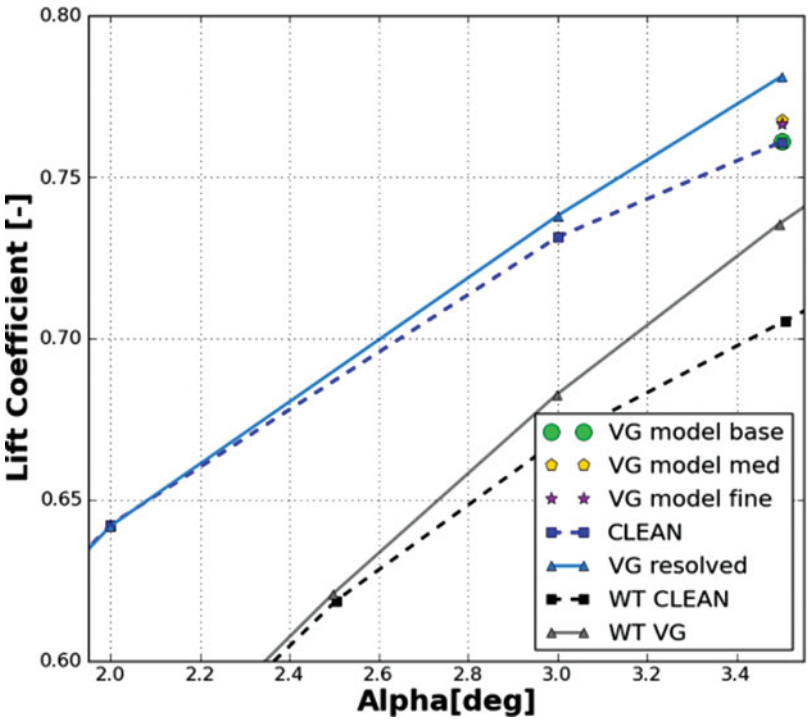

Figure 20. (Colour online) Lift polar obtained with TAU reduced-order VG model computed with different meshes.

the VG area, were also generated. Only un-deformed wing simulations at high angles of attack were performed using the VG model.

The resulting lift coefficient at $\alpha = 3.5°$ for different meshes is shown in Fig. 20. All the simulations converged to the set convergence criteria.

Analysis of the lift coefficient values indicates that the base mesh solution did not capture the impact of the VGs on the flow behaviour. On the other hand, mesh refinement allows for the vortices to be resolved and leads to a visible increase in the C_L value. However, the lift increase obtained is considerably smaller than in the resolved VG case, and further increase of the refinement level does not improve the results.

The skin friction coefficient plot in Fig. 21 shows the character of the surface flow on the upper wing surface for the fine mesh simulation at $\alpha = 3.5°$. Clear vortex traces can be identified downstream of the locations of the modelled VGs. Comparison of these results with the earlier observation from the resolved vanes indicates that the TAU VG model produces a much less energetic boundary layer behind the VGs, even though the separated flow region is, in fact, smaller.

The computed pressure distributions are shown in Fig. 22. The c_p values for the base mesh VG model are the same as for the clean wing simulations, which confirms the fact that there is no difference in the calculated force coefficients. The base mesh is too coarse for the vortex to be captured effectively; therefore, some level of refinement is clearly required.

The impact of the modelled VGs is clearly visible in the pressure distributions of the outboard sections when the refined grids are applied. Aft shock motion can be identified;

https://doi.org/10.1017/aer.2016.13 Published online by Cambridge University Press

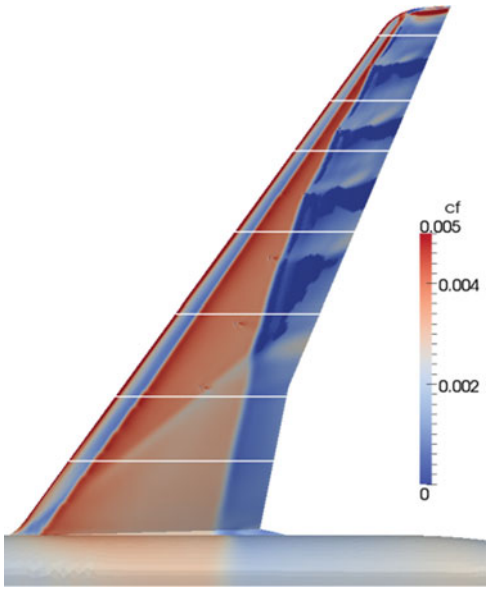

Figure 21. (Colour online) Skin friction distribution obtained with the TAU reduced-order VG model computed with fine mesh at $\alpha = 3.5°$.

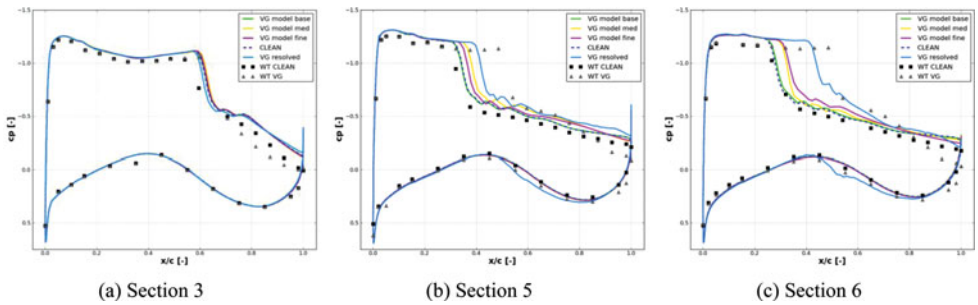

Figure 22. (Colour online) Pressure distributions obtained with the TAU reduced-order VG model computed with different meshes at $\alpha = 3.5$.

however, no clear pattern related to the mesh refinement level can be captured. Even though the VG model has clearly some influence on the flow behaviour, the obtained results are still closer to the clean wing results than to the resolved VG case. It is also worth noting that the lower surface pressures are virtually unaffected by application of the model, which is neither the case in the wind-tunnel experiments nor in the resolved VG simulations with the SSG model.

Despite the fact that the TAU VG model allowed some of the flow features induced by the VGs to be captured, and was the only method that resulted in a fully converged solution at high incidences, the C_L increase prediction offered by the model is not large enough. The specification of model parameters is somewhat ambiguous, and the obtained vortices are significantly weaker than those from other investigated approaches (Fig. 23). A number of additional tests, in which the model parameters (vane spacing, vortex core radius, etc.) were modified, did not lead to a significant improvement in results.

https://doi.org/10.1017/aer.2016.13 Published online by Cambridge University Press

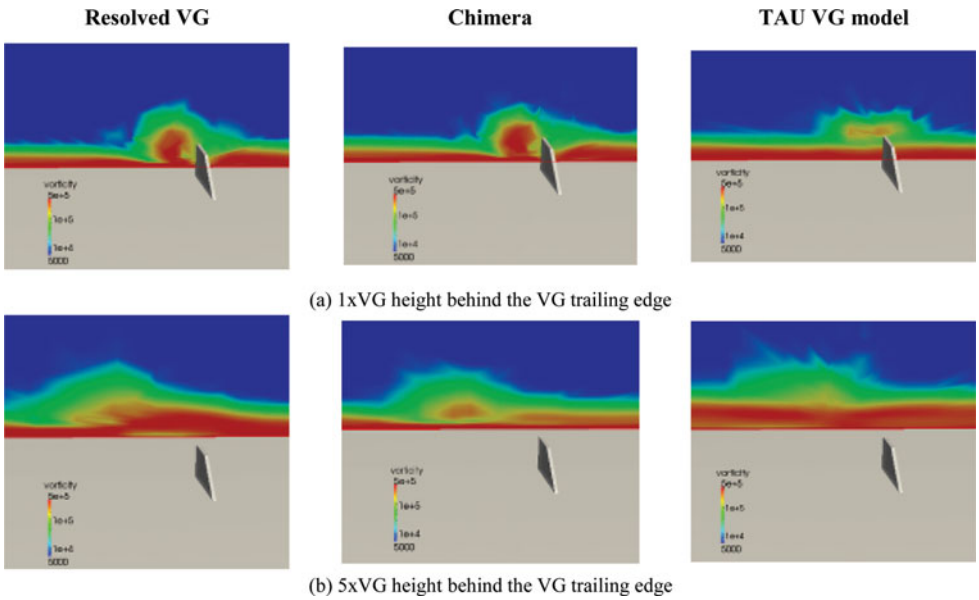

Figure 23. (Colour online) Vorticity contours at various distances behind the VG trailing edge. (a) 1xVG height behind the VG trailing edge. (b) 5xVG height behind the VG trailing edge.

Considering the analysis presented above and the complicated set-up procedure of the TAU VG model, it can be concluded that this approach is not yet mature enough for industrial application. With some improvements and additional tests, it is possible that the model could deliver a more promising performance.

6.0 CONCLUSIONS

This paper has presented work performed on the assessment of various VG modelling techniques that can be applied for simulations of transonic flows. Steady RANS simulations with the one-equation Spalart-Allmaras turbulence model and the SSG/LRR Reynolds-stress model (SSG) have been obtained for the clean wing configuration and for the wing with attached VGs. In addition, SSG simulations have been performed for alternative VG modelling techniques, the adaptation of Chimera overset meshes and the application of the reduced-order VG model available in TAU. Also, simulations taking into account the model deformation under the aerodynamic loading have been performed. The results of the simulations have been compared with wind-tunnel data acquired in test campaigns at the ARA TWT.

Out of the two turbulence models considered in the presented investigation, only the SSG model is able to capture the impact that the VGs have on the flow behaviour. In general, for the clean wing configuration, the SSG solutions give lift reduction at higher angles of attack, which is closer to the experimental data. This turbulence model is also able to capture, to some extent, the vortex trails and their interaction with the wing boundary layer, resulting in lift recovery when the VGs are simulated. However, none of the cases with VGs managed to converge to a stationary solution, which might indicate that there is a need for mesh improvement and/or application of an Unsteady Reynolds-Averaged Navier Stokes approach.

https://doi.org/10.1017/aer.2016.13 Published online by Cambridge University Press

Use of a Chimera method as an alternative technique to the fully resolved approach was also investigated. The Chimera method allows the VG geometry and required mesh refinement to be largely (but not totally) decoupled from the baseline grid. The presented results for a deformed wing show that there is potential in this approach. However, in some cases the offered solution is not satisfactory, as observed in the un-deformed case, in which the flow induced by the VG inside the Chimera block is not captured properly.

The only modelling technique that resulted in a satisfactory convergence with a VG array was the application of the TAU reduced-order VG model. Instead of modelling the VG vanes directly, this model inserts vortices into the flow based on a pre-defined set of parameters. Although this method offers great advantages, the current study shows that it has not yet reached a desired level of maturity.

The presented research has considerably increased the understanding of different approaches for modelling VGs. Various advantages and limitations of each approach have been identified; however, all methods have a limited industrial application. Nevertheless, only a small fraction of possibilities and strategies has been explored. Moreover, due to the complexity of the chosen reference data, a quantitative comparison of the studied methods proved to be challenging.

ACKNOWLEDGEMENTS

Study presented in this paper has been partially funded through a grant from the UK Aerospace Technology Institute (ATI) administered by the UK Technology Strategy Board (TSB).

REFERENCES

1. ROLSTON, S. High Reynolds number tools and techniques for civil aircraft design. *AIAA Paper 2001-2411*, June 2001.
2. ESDU. Vortex generators for control of shock-induced separation. Part 1: introduction and aerodynamics; ESDU transonic Data Memor. No. 93024, December 1993 (with Amendment A, February 1995).
3. BOOKER, C.D., ZHANG, X. and CHERNYSHENKO, S.I. Large-scale vortex generation modelling, *J Fluids Engineering*, 2011, **133**, (12), pp 121201.
4. JOUBERT, G., LE PAPE, A. and HUBERSON, S. Numerical study of flow separation control over a OA209 airfoil using deployable vortex generator, 49th AIAA Aerospace Sciences Meeting, 2011, Orlando, Florida, US.
5. ABBAS, A., DE VICENTE, J. and VALERO, E. Aerodynamic technologies to improve aircraft performance, *Aerospace Science and Technology*, 2013, **28**, (1), pp 100-132.
6. HAHN, M. Transonic flow over the N47-05 half-model: Part I – Analysis of numerical and experimental clean-wing data, ARA Contractor Report RAH00402/1, March 2014.
7. MARTINEAU, D.G. *et al.* Anisotropic hybrid mesh generation for industrial RANS applications, *AIAA Paper* 2006-0534, January 2006.
8. SCHWAMBORN, D., GERHOLD, T. and HEINRICH, R. The DLR TAU-code: Recent applications in research and industry. Proceedings of the European Conference on Computational Fluid Dynamics, ECCOMAS CFD 2006, 5-8 September 2006, Delft University of Technology, Egmond aan Zee, The Netherlands.
9. SPALART, P.R. and ALLMARAS, S.R. A one-equation turbulence model for aerodynamic flows, *La Recherché Aerospatiale*, 1994, **1**, pp 5-21.
10. CÉCORA, R.-D., RADESPIEL, R., EISFELD, B. and PROBST, A. Differential Reynolds-stress modeling for aeronautics, *AIAA J*, 2015, **53**, (3), pp 739-755.
11. ZASTAWNY, M. DRSM results for a flat plate boundary layer using TAU, ARA Contractor Report AAH00903/2, December 2013.

https://doi.org/10.1017/aer.2016.13 Published online by Cambridge University Press

12. ZASTAWNY, M. Transonic flow over the N47-05 half-model: Part II – Vortex generator study, ARA Contractor Report RAH00402/2, March 2014.
13. BENDER, E.E. *et al.* Vortex generator modelling for Navier-Stokes codes, 3rd Joint ASME/JSME Fluid engineering Conference, Paper No. FEDSM99-6919, July 1999, San Francisco, California, US.
14. TÖRNBLOM, O. and JOHANSSON, A.V. A Reynolds stress closure description of separation control with vortex generators in a plane asymmetric diffuser, *Physics of Fluids*, 2007, **19**, (11), pp 115108.

https://doi.org/10.1017/aer.2016.13 Published online by Cambridge University Press